

Article

Facile Preparation, Microstructure and Dielectric Properties of $\text{La}(\text{Cr}_{0.2}\text{Mn}_{0.2}\text{Fe}_{0.2}\text{Co}_{0.2}\text{Ni}_{0.2})\text{O}_3$ Perovskite High-Entropy Ceramics

Zhifeng Tian ^{1,*}, Ying Zhang ^{1,*}, Junzhan Zhang ¹ and Peng Shi ^{2,*}

¹ College of Materials Science and Engineering, Xi'an University of Architecture and Technology, Xi'an 710055, China

² Electronic Materials Research Laboratory, Key Laboratory of the Ministry of Education & International Center for Dielectric Research, School of Electronic and Information Engineering, Xi'an Jiaotong University, Xi'an 710049, China

* Correspondence: xayzhang@xauat.edu.cn (Y.Z.); spxjy@mail.xjtu.edu.cn (P.S.)

Abstract: Preparation and properties of $\text{La}(\text{Cr}_{0.2}\text{Mn}_{0.2}\text{Fe}_{0.2}\text{Co}_{0.2}\text{Ni}_{0.2})\text{O}_3$ high-entropy ceramics are investigated. $\text{La}(\text{Cr}_{0.2}\text{Mn}_{0.2}\text{Fe}_{0.2}\text{Co}_{0.2}\text{Ni}_{0.2})\text{O}_3$ high-entropy ceramics are prepared by a traditional two-step solid-state reaction method in air. $\text{La}(\text{Cr}_{0.2}\text{Mn}_{0.2}\text{Fe}_{0.2}\text{Co}_{0.2}\text{Ni}_{0.2})\text{O}_3$ single-phase powders are synthesized by calcining the mixed oxides at 1000 °C for 20 h. The high-entropy ceramics are sintered at 1350–1650 °C in a muffle furnace for 4 h by using the above powders. The phase compositions of the high-entropy ceramics at different temperatures are characterized by X-ray diffraction (XRD) with Cu K α radiation. A field-emission scanning electron microscope with energy-dispersive spectroscopy (EDS) is used to observe the microstructures and analyze the elemental distributions. The hardness and dielectric properties are measured and discussed.

Keywords: $\text{La}(\text{Cr}_{0.2}\text{Mn}_{0.2}\text{Fe}_{0.2}\text{Co}_{0.2}\text{Ni}_{0.2})\text{O}_3$; perovskite; high-entropy ceramics; hardness; dielectric properties



Citation: Tian, Z.; Zhang, Y.; Zhang, J.; Shi, P. Facile Preparation, Microstructure and Dielectric Properties of $\text{La}(\text{Cr}_{0.2}\text{Mn}_{0.2}\text{Fe}_{0.2}\text{Co}_{0.2}\text{Ni}_{0.2})\text{O}_3$ Perovskite High-Entropy Ceramics. *Crystals* **2022**, *12*, 1756. <https://doi.org/10.3390/cryst12121756>

Academic Editors: Maria Gazda and Dmitry Medvedev

Received: 26 October 2022

Accepted: 2 December 2022

Published: 4 December 2022

Publisher's Note: MDPI stays neutral with regard to jurisdictional claims in published maps and institutional affiliations.



Copyright: © 2022 by the authors. Licensee MDPI, Basel, Switzerland. This article is an open access article distributed under the terms and conditions of the Creative Commons Attribution (CC BY) license (<https://creativecommons.org/licenses/by/4.0/>).

1. Introduction

High-entropy materials, one of the most influential concepts in material science in the past ten years, refer to multicomponent solid solutions formed by five or more components [1]. The first high-entropy ceramic, $(\text{Mg}_{0.2}\text{Co}_{0.2}\text{Ni}_{0.2}\text{Cu}_{0.2}\text{Zn}_{0.2})\text{O}$ with regular Fm-3m rock-salt structure, was reported by Rost et al. in 2015 [2]. Since then, a series of high-entropy ceramics, including high-entropy oxide ceramics with fluorite [3–6], perovskite [7–9], spinel structures [10,11] and so on, as well as nonoxide high-entropy ceramics, such as borides [12–14], carbides [15–18], nitrides [19], and silicides [20,21], have been synthesized. Among them, perovskite-structure high-entropy oxides have excellent physical properties for applications in many different fields [7–9]. For example, they can be used as cathode materials for solid-oxide fuel cells (SOFCs) [22,23], dielectrics [24,25], and ferroelectric and multiferroic materials [26–28].

Lanthanum chromate (LaCrO_3) has a typical perovskite crystal structure, good chemical resistance, and chemical and physical stability at high temperature, but its sintering properties are poor [29,30]. In the current research reports, most of them improve the sintering and high-temperature properties of LaCrO_3 ceramics by doping the A and B sites and adding sintering aids [31–34]. For example, Ga et al. and Luo et al. [35,36] prepared highly stable composite negative-temperature coefficient (NTC) ceramics by introducing perovskite (LaCrO_3) into certain spinel oxides. Therefore, in this study when designing perovskite-type high-entropy oxides, the active transition metal elements Cr, Mn, Fe, Co, and Ni with close ionic radii were selected for the B site. Theoretically, the highest configurational entropy is obtained for some materials when all the elements

in a sublattice have the same atomic fraction [21,37]. In 2021, Guo et al. [38] reported that $\text{La}(\text{Cr}_{0.2}\text{Mn}_{0.2}\text{Fe}_{0.2}\text{Co}_{0.2}\text{Ni}_{0.2})\text{O}_3$ perovskite high-entropy powders prepared by the coprecipitation and combined with calcination method presented good rate properties for the application in supercapacitors. Vladimir et al. [39] reported that $\text{La}(\text{Cr}_{0.2}\text{Mn}_{0.2}\text{Fe}_{0.2}\text{Co}_{0.2}\text{Ni}_{0.2})\text{O}_3$ perovskite high-entropy ceramics sintered at 1300 °C for 10 h in air showed a single phase with a perovskite-like structure. It also exhibited good DC conductivities at room temperature for the application in SOFC. At high temperatures, the transition metal ions exhibit a variety of oxidation states, accompanied by a variety of charge disproportionation, such as $\text{Mn}^{4+} + \text{Ni}^{2+} \rightarrow \text{Mn}^{3+} + \text{Ni}^{3+}$ [40]. However, there are few reports on the microstructure and dielectric properties of $\text{La}(\text{Cr}_{0.2}\text{Mn}_{0.2}\text{Fe}_{0.2}\text{Co}_{0.2}\text{Ni}_{0.2})\text{O}_3$ perovskite high-entropy ceramics prepared at higher temperatures (>1300 °C).

In this study, $\text{La}(\text{Cr}_{0.2}\text{Mn}_{0.2}\text{Fe}_{0.2}\text{Co}_{0.2}\text{Ni}_{0.2})\text{O}_3$ perovskite high-entropy ceramics were prepared at high temperatures of 1350–1650 °C. Next, phase composition and the microstructure of $\text{La}(\text{Cr}_{0.2}\text{Mn}_{0.2}\text{Fe}_{0.2}\text{Co}_{0.2}\text{Ni}_{0.2})\text{O}_3$ perovskite high-entropy ceramics sintered at different temperatures were investigated. Finally, the density, hardness, and dielectric properties of $\text{La}(\text{Cr}_{0.2}\text{Mn}_{0.2}\text{Fe}_{0.2}\text{Co}_{0.2}\text{Ni}_{0.2})\text{O}_3$ high-entropy ceramics were analyzed.

2. Materials and Methods

In this work, $\text{La}(\text{Cr}_{0.2}\text{Mn}_{0.2}\text{Fe}_{0.2}\text{Co}_{0.2}\text{Ni}_{0.2})\text{O}_3$ high-entropy ceramics were prepared by a typical two-step solid-state method using the analytical-grade metal oxides La_2O_3 (AR, $\geq 99.0\%$), Cr_2O_3 (AR, $\geq 99.0\%$), Co_2O_3 (AR, $\geq 99.0\%$), Fe_2O_3 (AR, $\geq 99.0\%$), MnO_2 (AR, $\geq 99.0\%$), and Ni_2O_3 (AR, $\geq 99.0\%$) as raw materials. Firstly, oxide powders were weighed according to the stoichiometric ratio of $\text{La}(\text{Cr}_{0.2}\text{Mn}_{0.2}\text{Fe}_{0.2}\text{Co}_{0.2}\text{Ni}_{0.2})\text{O}_3$ and then ball-milled with alcohol and agate balls in a planetary mill for 12 h. Then, the slurry was dried and passed through a 150 μm sieve. The above powder mixture was pressed into a disc and then calcined at 900–1200 °C in a muffle furnace (KSL-1700X, Kejing Company, Hefei, China) for 20 h in air. The synthesized disc was then crushed, pulverized, ball-milled, and passed through a 150 μm sieve again to obtain homogeneous powders. The ceramic discs of 10 mm in diameter and 2 mm in thickness were pressed at 25 MPa with 3 wt% polyvinyl acetate (PVA) as binder. The green bodies were sintered at 1350–1650 °C for 4 h with a heating rate of 5 °C·min⁻¹ and cooled naturally.

The phase compositions of the synthesized powders and sintered high-entropy ceramics were analyzed by a high-resolution X-ray diffraction (XRD) (Bruker D8 Advance, $\text{CuK}\alpha$ target with $\lambda = 0.15418$ nm, Bruker, Karlsruhe, Germany). The morphology and element distribution of the powders and morphology of the high-entropy ceramics were characterized by SEM and EDS (FEI Quanta 250 FEG microscope and EDS detector). The particle size and the distribution of the powders were calculated using Image-Pro software. The apparent porosity and bulk density of high-entropy ceramics were obtained according to the Archimedes method. The theoretical density of high-entropy ceramics was calculated based on the lattice parameters obtained from XRD patterns and the molecular weight of the stoichiometric ratio of $\text{La}(\text{Cr}_{0.2}\text{Mn}_{0.2}\text{Fe}_{0.2}\text{Co}_{0.2}\text{Ni}_{0.2})\text{O}_3$. The relative density was calculated by dividing the measured sample bulk density by the theoretical density. The HV-2000 A micro-Vickers hardness tester (Shanghai Qinming, Shanghai, China) was employed to characterize the hardness of the high-entropy ceramics. The peak load was 19.61 N, and the pressure was maintained for 10 s. Temperature-dependent dielectric properties, at a frequency of 10 kHz of high-entropy ceramics with silver-pasted electrodes, were measured with an Agilent 4980A LCR meter when the samples were heated from 20 °C to 150 °C at a rate of 2 °C·min⁻¹.

3. Results

3.1. Phase Composition and Microstructural Analysis

Figure 1 shows XRD patterns of $\text{La}(\text{Cr}_{0.2}\text{Mn}_{0.2}\text{Fe}_{0.2}\text{Co}_{0.2}\text{Ni}_{0.2})\text{O}_3$ high-entropy powders calcined at different temperatures. It can be seen that the prepared high-entropy powders are consistent with the orthorhombic perovskite structure with the space group $Pnma$ (62),

and no additional peaks are observed in any of the prepared samples. The diffraction peaks match well with JCPDS # 89–0478 of pure LaCrO_3 at room temperature [41]. It shows that the solid-state reaction at 1000°C for 20 h provides sufficient time for atomic diffusion, thus forming a highly symmetrical perovskite phase-disordered solid solution [42]. According to the relationship between Gibbs free energy (ΔG_{mix}) and temperature, ΔG_{mix} decreases with increasing temperature, which stabilizes the high-entropy system. Therefore, 1000°C is determined as an appropriate temperature for calcining powders in the first step. Additionally, the high sintering activity of the powders obtained at 1000°C facilitates the formation of dense bulk ceramics at a higher sintering temperature.

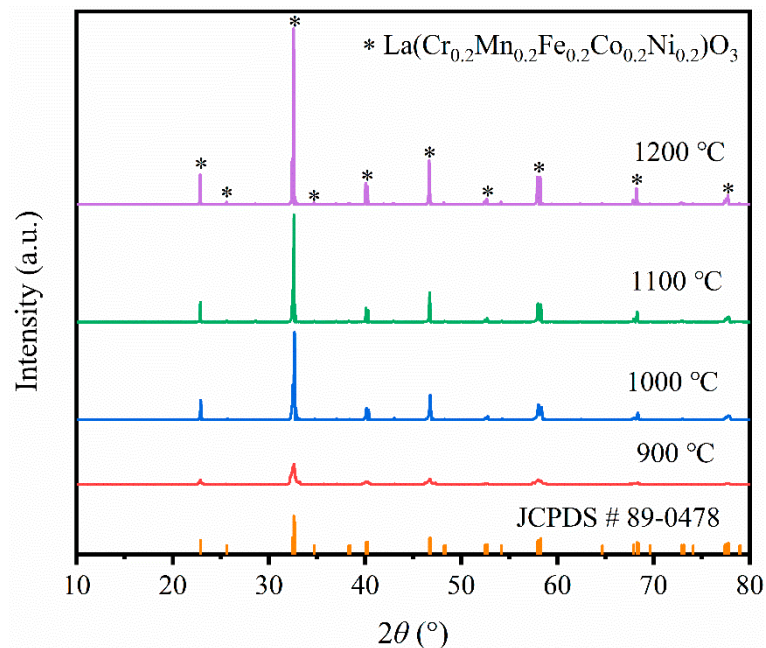


Figure 1. XRD patterns of $\text{La}(\text{Cr}_{0.2}\text{Mn}_{0.2}\text{Fe}_{0.2}\text{Co}_{0.2}\text{Ni}_{0.2})\text{O}_3$ powders calcined at different temperatures. * assigned phase symbol of peaks of $\text{La}(\text{Cr}_{0.2}\text{Mn}_{0.2}\text{Fe}_{0.2}\text{Co}_{0.2}\text{Ni}_{0.2})\text{O}_3$.

For perovskite oxides, Goldschmidt [43] proposed in 1926 that the “tolerance factor” can be used to predict the single phase of perovskite, which can be calculated using Equation (1):

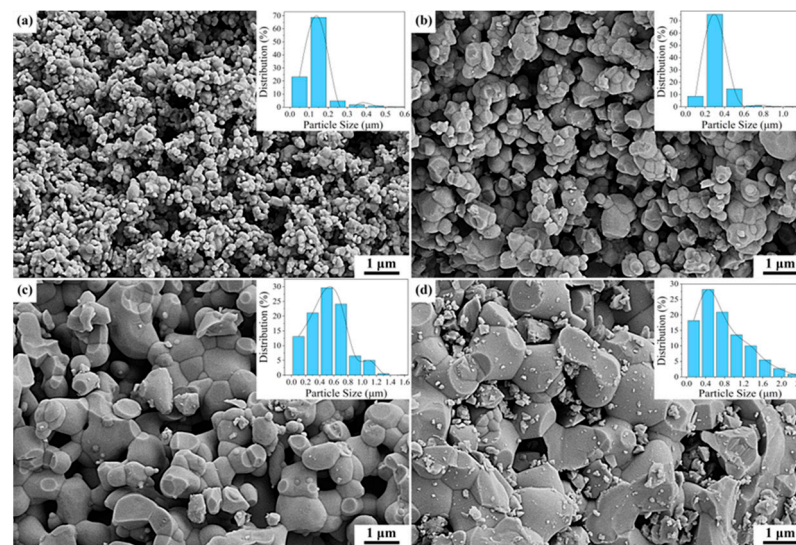
$$t = \frac{R_A + R_O}{\sqrt{2}(R_B + R_O)} \quad (1)$$

where R_A and R_B are the ionic radii of the cation at A site and B site, respectively, and R_O is the radius of the oxygen ion. In the case of multiple cations at a specific site, an average of the ionic radii is considered [7]. In an ideal case, $t \approx 1$ is perhaps a necessary but not sufficient condition for the formation of a cubic structure; when $t > 1.0$, a tetragonal or hexagonal structure may be formed [44]; and when $t < 1.0$, an orthorhombic or rhombohedral structure may be formed, especially for systems with smaller A-site cations or bigger B-site cations [45]. The oxidation state, coordination number (CN), and corresponding cation radius (r_c) [45] of each element of $\text{La}(\text{Cr}_{0.2}\text{Mn}_{0.2}\text{Fe}_{0.2}\text{Co}_{0.2}\text{Ni}_{0.2})\text{O}_3$ high-entropy ceramic are shown in Table 1. It can be seen from Table 1 that $t \approx 0.966$, and a single-phase perovskite high-entropy ceramic material can be formed. This is consistent with the conclusion reported by Jiang et al. [7], that stable, single-phase perovskite high-entropy ceramics are formed when $t \approx 1$. The slightly smaller t value may be due to lattice distortion caused by the combination of various elements in the high-entropy material.

Table 1. Oxidation state, coordination number (CN), and corresponding cationic radius (r_c) (data from Shannon).

Element	Oxidation	CN	r_c (Å)
La	+3	XII	1.36
Cr	+3	VI	0.615
Co	+3	VI	0.545
Fe	+3	VI	0.55
Mn	+4	VI	0.53
Ni	+3	VI	0.56
O	−2	VI	1.40

Figure 2 shows SEM images of $\text{La}(\text{Cr}_{0.2}\text{Mn}_{0.2}\text{Fe}_{0.2}\text{Co}_{0.2}\text{Ni}_{0.2})\text{O}_3$ powders calcined at different temperatures. It can be seen that the grain size increases obviously with the increase in calcination temperature. The powders calcined at 900 °C have poor dispersibility and form small grain agglomerates due to the small grain size. The grain size of the powders calcined at 1000 °C increases slightly, and there is no obvious agglomeration. Compared with Figure 2a, the grain-size distribution is relatively more uniform, and the grain size is in the range of 200–400 nm. When calcination temperature increases to 1100 °C and 1200 °C, the grain size of $\text{La}(\text{Cr}_{0.2}\text{Mn}_{0.2}\text{Fe}_{0.2}\text{Co}_{0.2}\text{Ni}_{0.2})\text{O}_3$ powders increases obviously, showing a large agglomeration state. In addition, a wider particle-size distribution can be found.

**Figure 2.** SEM images of $\text{La}(\text{Cr}_{0.2}\text{Mn}_{0.2}\text{Fe}_{0.2}\text{Co}_{0.2}\text{Ni}_{0.2})\text{O}_3$ powders calcined at different temperatures. (a) 900 °C; (b) 1000 °C; (c) 1100 °C; (d) 1200 °C. (the insert graphs are the particle size and the distribution of the powders calcined at different temperatures).

The XRD results of the crystal structure of $\text{La}(\text{Cr}_{0.2}\text{Mn}_{0.2}\text{Fe}_{0.2}\text{Co}_{0.2}\text{Ni}_{0.2})\text{O}_3$ high-entropy ceramics are shown in Figure 3. It can be seen that the diffraction peaks of $\text{La}(\text{Cr}_{0.2}\text{Mn}_{0.2}\text{Fe}_{0.2}\text{Co}_{0.2}\text{Ni}_{0.2})\text{O}_3$ high-entropy ceramics sintered at 1350 °C and 1400 °C correspond well to the standard card of LaCrO_3 (JCPDS # 89-0478). When sintering temperatures increase to 1450 °C and 1500 °C, a small amount of the second-phase LaMnO_3 appears. When the sintering temperature is 1550 °C, in addition to the presence of the second-phase LaMnO_3 , the chromium-containing oxides start to volatilize and the peaks contain some mixed peaks of chromium oxide and cobalt oxides, such as CrO_2 and Co_3O_4 . When the sintering temperature further increases to 1600 °C, the LaMnO_3 peak disappears and new peaks of CrO_3 appear. When the sintering temperature reaches 1650 °C, the diffraction peaks match well with the standard card, while the peaks shift to the right slightly. This may be due to the formation of the transient liquid phase by doping Co at a high temperature (1650 °C), which promotes sintering [46].

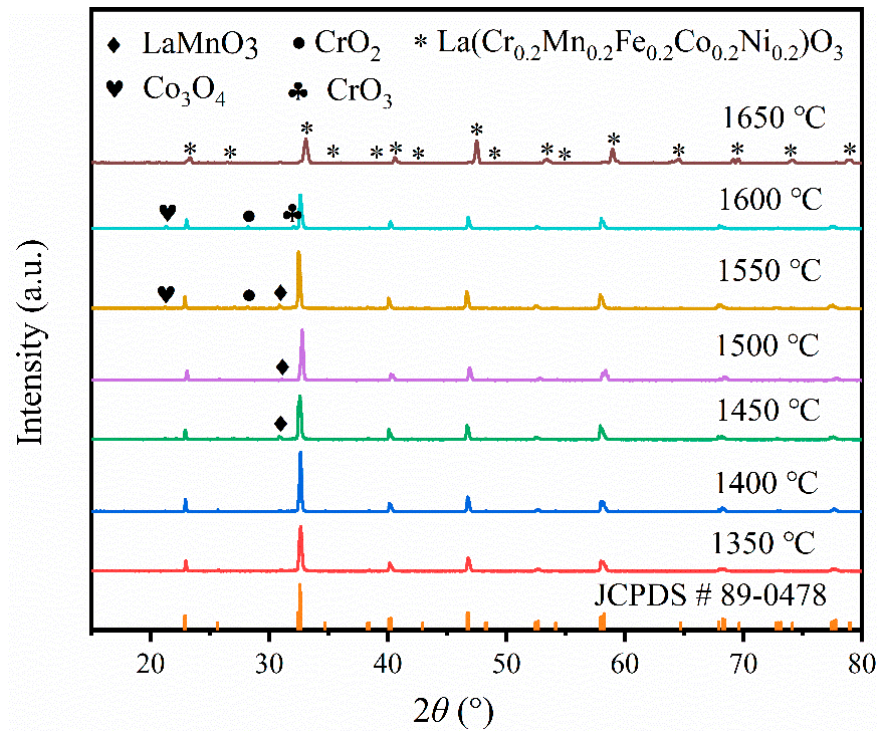


Figure 3. XRD patterns of $\text{La}(\text{Cr}_{0.2}\text{Mn}_{0.2}\text{Fe}_{0.2}\text{Co}_{0.2}\text{Ni}_{0.2})\text{O}_3$ high-entropy ceramics sintered at different temperatures.

Figure 4 shows SEM images of $\text{La}(\text{Cr}_{0.2}\text{Mn}_{0.2}\text{Fe}_{0.2}\text{Co}_{0.2}\text{Ni}_{0.2})\text{O}_3$ high-entropy ceramics sintered at different temperatures. The results show that a relatively dense microstructure is obtained with a grain size of about $1.6 \mu\text{m}$ when $\text{La}(\text{Cr}_{0.2}\text{Mn}_{0.2}\text{Fe}_{0.2}\text{Co}_{0.2}\text{Ni}_{0.2})\text{O}_3$ high-entropy ceramic is sintered at $1350 \text{ }^\circ\text{C}$. To further verify the uniformity of element distribution, $\text{La}(\text{Cr}_{0.2}\text{Mn}_{0.2}\text{Fe}_{0.2}\text{Co}_{0.2}\text{Ni}_{0.2})\text{O}_3$ high-entropy ceramics sintered at $1350 \text{ }^\circ\text{C}$ are analyzed with EDS. As shown in Figure 5a, all six elements are uniformly distributed without any element segregation or aggregation. The atomic ratios obtained by semiquantitative elemental analysis, which are almost equal to the designed perovskite composition, indicate that there is no obvious composition change during the sintering process. Based on the analysis results, the atomic fractions of each element are shown in Figure 5b. It can be seen from the inset that the ratio of atom and mass of the five elements is about 5%, and the variation is $\pm 0.5\%$. The atomic and mass fractions of the five elements are extremely close, providing further evidence for the equiatomic composition of Cr^{3+} , Mn^{4+} , Fe^{3+} , Co^{3+} , and Ni^{3+} at the B site (ABO_3). When the sintering temperature is $1350 \text{ }^\circ\text{C}$, it can be seen that the grain size of the high-entropy ceramics is relatively small. When the sintering temperature increases to $1400\text{--}1450 \text{ }^\circ\text{C}$, some pores appear and the density decreases in the microstructure of $\text{La}(\text{Cr}_{0.2}\text{Mn}_{0.2}\text{Fe}_{0.2}\text{Co}_{0.2}\text{Ni}_{0.2})\text{O}_3$ high-entropy ceramics. The grain size increases from $1.6 \mu\text{m}$ to about $2.6 \mu\text{m}$. When the sintering temperatures are higher than $1500 \text{ }^\circ\text{C}$ ($1500\text{--}1600 \text{ }^\circ\text{C}$), the second phase (small white particles) first precipitates at the grain boundary and then precipitates along the surface, which is consistent with the XRD results. Moreover, there are no obvious pores observed in SEM images and the grain size further increases from $8.6 \mu\text{m}$ to $17.4 \mu\text{m}$. The grain size of $\text{La}(\text{Cr}_{0.2}\text{Mn}_{0.2}\text{Fe}_{0.2}\text{Co}_{0.2}\text{Ni}_{0.2})\text{O}_3$ high-entropy ceramics grows significantly with a clear grain boundary and the grains are closely adjacent to each other.

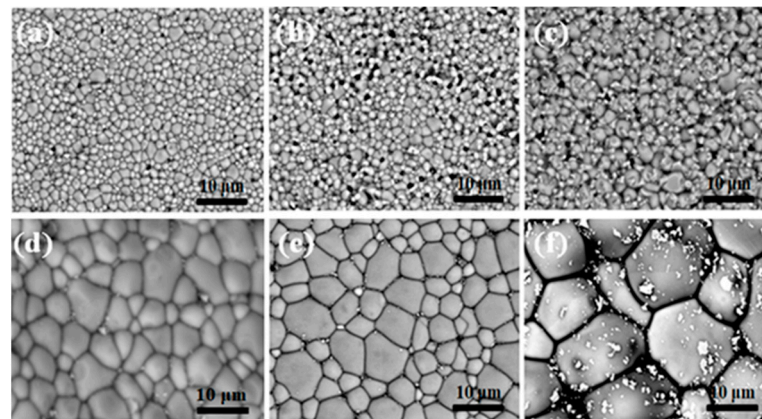


Figure 4. SEM images of $\text{La}(\text{Cr}_{0.2}\text{Mn}_{0.2}\text{Fe}_{0.2}\text{Co}_{0.2}\text{Ni}_{0.2})\text{O}_3$ high-entropy ceramics sintered at different temperatures. (a) 1350 °C; (b) 1400 °C; (c) 1450 °C; (d) 1500 °C; (e) 1550 °C; (f) 1600 °C.

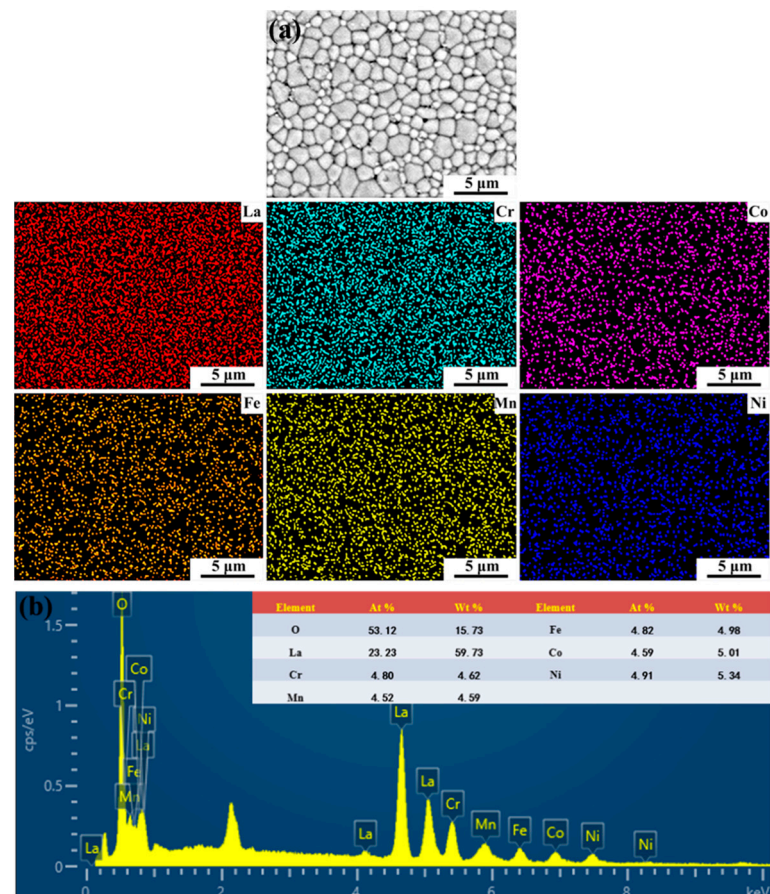


Figure 5. SEM image, EDS element mapping, and atomic and mass fraction of $\text{La}(\text{Cr}_{0.2}\text{Mn}_{0.2}\text{Fe}_{0.2}\text{Co}_{0.2}\text{Ni}_{0.2})\text{O}_3$ high-entropy ceramics sintered at 1350 °C. (a) SEM image; (b) EDS element mapping.

When the sintering temperature reaches 1650 °C (Figure 6), pores and liquid phases can be found in $\text{La}(\text{Cr}_{0.2}\text{Mn}_{0.2}\text{Fe}_{0.2}\text{Co}_{0.2}\text{Ni}_{0.2})\text{O}_3$ high-entropy ceramics through the local magnification of the SEM images. When the temperature reaches 1650 °C, the volatilization of Cr in the ceramic matrix leads to the formation of pores, and the doping of Co forms a transient liquid phase to promote sintering [47].

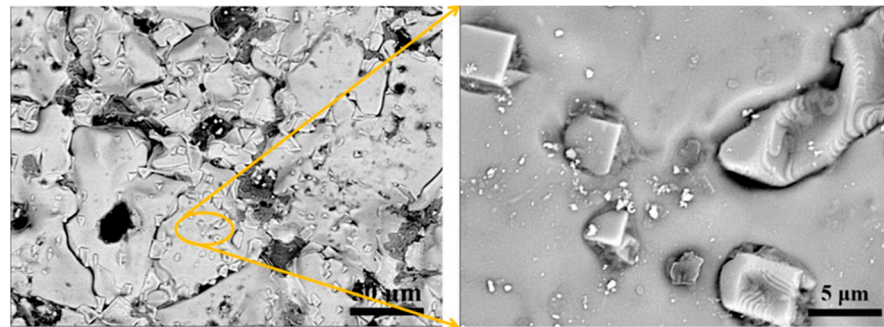


Figure 6. SEM images of $\text{La}(\text{Cr}_{0.2}\text{Mn}_{0.2}\text{Fe}_{0.2}\text{Co}_{0.2}\text{Ni}_{0.2})\text{O}_3$ high-entropy ceramics sintered at 1650 °C.

3.2. Density, Apparent Porosity, and Hardness

Figure 7 shows the relative density, apparent porosity, and hardness of $\text{La}(\text{Cr}_{0.2}\text{Mn}_{0.2}\text{Fe}_{0.2}\text{Co}_{0.2}\text{Ni}_{0.2})\text{O}_3$ high-entropy ceramics sintered at different temperatures. It can be seen that when sintering temperature is 1350 °C, the relative density is 93.0%, apparent porosity is 2.2%, and the hardness is 14.7 GPa. When the sintering temperature is 1400 °C, relative density decreases to the minimum (88.4%), apparent porosity increases to the maximum (5.6%), and the hardness is 14.4 GPa. When the sintering temperature increases to 1450 °C, the hardness reaches the minimum of 13.2 GPa. When the sintering temperature increases from 1450 °C to 1500 °C, the relative density increases from 88.7% to 96.8%, an increase of 8.1%. When the sintering temperature increases from 1500 °C to 1600 °C, the relative densities of high-entropy ceramics increase continuously. When the sintering temperature is 1600 °C, the relative density reaches the maximum of 99.5% and the porosity reaches the minimum of 1.0%. When the sintering temperature continues to increase from 1600 °C to 1650 °C, the relative density decreases to 92.1%. The change law of apparent porosity is just the opposite. The hardness values first decrease and then increase. When the sintering temperature is 1650 °C, the hardness value reaches the maximum of 18.7 GPa.

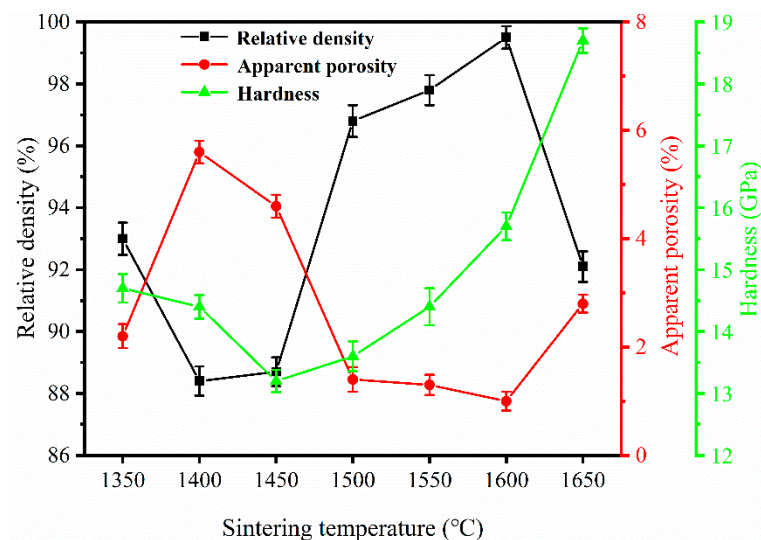


Figure 7. Relative density, apparent porosity, and hardness of $\text{La}(\text{Cr}_{0.2}\text{Mn}_{0.2}\text{Fe}_{0.2}\text{Co}_{0.2}\text{Ni}_{0.2})\text{O}_3$ high-entropy ceramics sintered at different temperatures.

3.3. Dielectric Properties

The temperature dependence of dielectric constant and dielectric loss of $\text{La}(\text{Cr}_{0.2}\text{Mn}_{0.2}\text{Fe}_{0.2}\text{Co}_{0.2}\text{Ni}_{0.2})\text{O}_3$ high-entropy ceramics sintered at different temperatures are shown in Figure 8, respectively. It can be seen that $\text{La}(\text{Cr}_{0.2}\text{Mn}_{0.2}\text{Fe}_{0.2}\text{Co}_{0.2}\text{Ni}_{0.2})\text{O}_3$ high-entropy ceramics have a giant dielectric constant, which is significantly larger than that of pure LaCrO_3 ceramics (the dielectric constant is about 1500 when the test temperature is 40 °C [40]). The higher dielectric constant may be obtained by the lattice distortion, which is often caused by

multielement doping [37,48]. In the low-frequency region, the dipole orientation polarization is the main reason for the higher dielectric constant, while in the high-frequency region, the dipole cannot be alternating with the electric field. With a further increase in frequency, the dipole oscillation induces polarization to stop and the partial spin polarization induced by the elemental solid solution produces the higher dielectric constant [49–51]. The dielectric constant increases with the increase in the test temperature, which is consistent with the results reported by Boudad et al. [52] and Coşkun et al. [53] on the dielectric properties of doped LaCrO_3 . The increased dielectric constant should be attributed to strong effects of the hopping of small polarons and carriers at the grain boundary, especially for the doping system [52,53]. The dielectric constant of the sample sintered at 1350°C increases rapidly with the increase in the test temperature. In addition, when the test temperature is $20\text{--}120^\circ\text{C}$, the dielectric loss increases continuously, and when the test temperature is higher than 120°C , the dielectric loss shows a decreasing trend. For the samples sintered at $1400\text{--}1550^\circ\text{C}$, the dielectric constant increases with the increase in sintering temperature, which is consistent with the increasing trend of relative density in Figure 7. The dielectric loss shows a different increase trend with the increase in test temperature. This is due to the presence of many point defects (such as vacancies, substituted atoms, and interstitial atoms) in multielement, high-entropy solid solutions that can act as polarization centers and as local stresses caused by lattice disorder that can suppress dipole reorientation under alternating electric fields, thereby increasing the dielectric loss in the material [54–57]. When the sintering temperature is further increased to 1600°C , the dielectric constant of the samples is significantly lower than those of high-entropy ceramics sintered at 1500°C and 1550°C at the same test temperature, which may be related to the jumping of oxygen vacancies due to the volatilization of elements, such as Cr and Co in the second phase of the sample. It affects the consistency of the ceramic matrix, which is also one of the factors affecting the dielectric constant. This is consistent with the results of XRD and SEM testing.

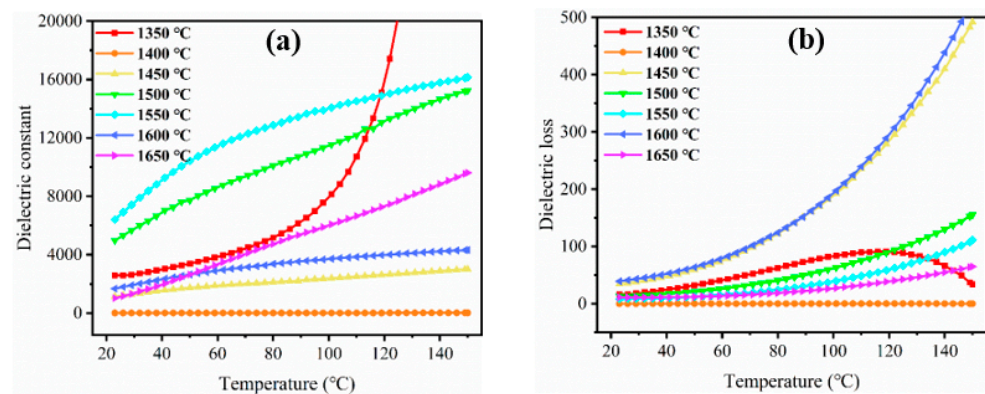


Figure 8. Temperature dependence of dielectric constant (a) and dielectric loss of (b) $\text{La}(\text{Cr}_{0.2}\text{Mn}_{0.2}\text{Fe}_{0.2}\text{Co}_{0.2}\text{Ni}_{0.2})\text{O}_3$ high-entropy ceramics at 10 kHz.

4. Conclusions

The phase composition, microstructure, hardness, and dielectric properties of $\text{La}(\text{Cr}_{0.2}\text{Mn}_{0.2}\text{Fe}_{0.2}\text{Co}_{0.2}\text{Ni}_{0.2})\text{O}_3$ perovskite high-entropy ceramics prepared through a two-step solid-state reaction technique were investigated. When the sintering temperatures were 1350°C and 1400°C , the phase of $\text{La}(\text{Cr}_{0.2}\text{Mn}_{0.2}\text{Fe}_{0.2}\text{Co}_{0.2}\text{Ni}_{0.2})\text{O}_3$ high-entropy ceramic presented a pure, single-perovskite structure. The relative density reached 93.0% and 88.4%, and the hardness reached 14.7 GPa and 14.4 GPa, respectively. When the sintering temperature increased to $1450\text{--}1600^\circ\text{C}$, the pure perovskite structure became unstable and the second-phase precipitates appeared in the XRD and SEM results. When the sintering temperature increased to the range of $1450\text{--}1600^\circ\text{C}$, the relative density and hardness of the high-entropy ceramics increased with the increase in sintering temperature. Furthermore, the dielectric constant increased with the increase in test temperature, showing excellent mechanical and dielectric properties. These results indicate that

La(Cr_{0.2}Mn_{0.2}Fe_{0.2}Co_{0.2}Ni_{0.2})O₃ high-entropy ceramic is a potential dielectric material that can be utilized at high temperatures.

Author Contributions: Formal analysis, Y.Z., J.Z. and P.S.; investigation, P.S. and Z.T.; writing—original draft preparation, Z.T. and P.S.; writing—review and editing, Z.T., P.S. and J.Z.; supervision: Y.Z. and P.S. All authors have read and agreed to the published version of the manuscript.

Funding: This research was funded by the national key research and development program (No. SQ2022FYB3200038) and the key research and development program of Shaanxi (No. 2020SF-426 and No. 2021GY-295).

Institutional Review Board Statement: Not applicable.

Informed Consent Statement: Not applicable.

Data Availability Statement: Not applicable.

Acknowledgments: We appreciate the support from the International Joint Laboratory for Micro/Nano Manufacturing and Measurement Technologies of Xi'an Jiaotong University.

Conflicts of Interest: The authors declare no conflict of interest.

References

1. Yeh, J.W.; Chen, S.K.; Lin, S.J.; Gan, J.Y.; Chin, T.S.; Shun, T.T.; Tsau, C.H.; Chang, S.Y. Nanostructured High-Entropy Alloys with Multiple Principal Elements: Novel Alloy Design Concepts and Outcomes. *Adv. Eng. Mater.* **2004**, *6*, 299–303. [\[CrossRef\]](#)
2. Rost, C.M.; Sachet, E.; Borman, T.; Moballegh, A.; Dickey, E.C.; Hou, D.; Jones, J.L.; Curtarolo, S.; Maria, J. Entropy-stabilized oxides. *Nat. Commun.* **2015**, *6*, 8485. [\[CrossRef\]](#)
3. Gild, J.; Samiee, M.; Braun, J.L.; Harrington, T.; Vega, H.; Hopkins, P.E.; Vecchio, K.; Luo, J. High-entropy fluorite oxides. *J. Eur. Ceram. Soc.* **2018**, *38*, 3578–3584. [\[CrossRef\]](#)
4. Wang, D.; Jiang, S.; Duan, C.; Mao, J.; Qi, X. Spinel-structured high entropy oxide (FeCoNiCrMn)₃O₄ as anode towards superior lithium storage performance. *J. Alloys Compd.* **2020**, *844*, 156–158. [\[CrossRef\]](#)
5. Wright, A.J.; Wang, Q.; Hu, C.; Yeh, Y.; Chen, R.; Luo, J. Single-phase duodenary high-entropy fluorite/pyrochlore oxides with an order-disorder transition. *Acta Mater.* **2021**, *211*, 116858. [\[CrossRef\]](#)
6. Zhu, J.; Meng, X.; Xu, J.; Zhang, P.; Lou, Z.; Reece, M.J.; Gao, F. Ultra-low thermal conductivity and enhanced mechanical properties of high-entropy rare earth niobates (RE₃NbO₇, RE = Dy, Y, Ho, Er, Yb). *J. Eur. Ceram. Soc.* **2021**, *41*, 1052–1057. [\[CrossRef\]](#)
7. Jiang, S.; Hu, T.; Gild, J.; Zhou, N.; Nie, J.; Qin, M.; Harrington, T.; Vecchio, K.; Luo, J. A new class of high-entropy perovskite oxides. *J. Scr. Mater.* **2018**, *142*, 116–120. [\[CrossRef\]](#)
8. Zheng, Y.; Zou, M.; Zhang, W.; Yi, D.; Lan, J.; Nan, C.; Lin, Y. Electrical and thermal transport behaviours of high-entropy perovskite thermoelectric oxides. *J. Adv. Ceram.* **2021**, *10*, 377–384. [\[CrossRef\]](#)
9. Chen, L.; Li, B.; Guo, J.; Zhu, Y.; Feng, J. High-entropy perovskite RETa₃O₉ ceramics for high-temperature environmental/thermal barrier coatings. *J. Adv. Ceram.* **2022**, *11*, 556–569. [\[CrossRef\]](#)
10. Wang, J.; Stenzel, D.; Azmi, R.; Najib, S.; Breitung, B. Spinel to Rock-Salt Transformation in High Entropy Oxides with Li Incorporation. *Electrochem* **2020**, *1*, 60–74. [\[CrossRef\]](#)
11. Ma, J.; Zhao, B.; Xiang, H.; Dai, F.Z.; Liu, Y.; Zhang, R.; Zhou, Y. High-entropy spinel ferrites MFe₂O₄ (M = Mg, Mn, Fe, Co, Ni, Cu, Zn) with tunable electromagnetic properties and strong microwave absorption. *J. Adv. Ceram.* **2022**, *11*, 754–768. [\[CrossRef\]](#)
12. Gild, J.; Zhang, Y.; Harrington, T.; Jiang, S.; Hu, T.; Quinn, M.C.; Mellor, W.M.; Zhou, N.; Vecchio, K.; Luo, J. High-Entropy Metal Diborides: A New Class of High-Entropy Materials and a New Type of Ultrahigh Temperature Ceramics. *Sci. Rep.* **2016**, *6*, 37946. [\[CrossRef\]](#) [\[PubMed\]](#)
13. Liu, D.; Liu, H.; Ning, S.; Chu, Y. Chrysanthemum-like high-entropy diboride nanoflowers: A new class of high-entropy nanomaterials. *J. Adv. Ceram.* **2020**, *9*, 339–348. [\[CrossRef\]](#)
14. Zhao, P.; Zhu, J.; Zhang, Y.; Shao, G.; Wang, H.; Li, M.; Liu, W.; Fan, B.; Xu, H.; Lu, H.; et al. A novel high-entropy monoboride (Mo_{0.2}Ta_{0.2}Ni_{0.2}Cr_{0.2}W_{0.2})B with superhardness and low thermal conductivity. *Ceram. Int.* **2020**, *46*, 26626–26631. [\[CrossRef\]](#)
15. Sarker, P.; Harrington, T.; Toher, C.; Oses, C.; Samiee, M.; Maria, J.P.; Brenner, D.W.; Vecchio, K.S.; Curtarolo, S. High-entropy high-hardness metal carbides discovered by entropy descriptors. *Nat. Commun.* **2018**, *9*, 4980–4989. [\[CrossRef\]](#) [\[PubMed\]](#)
16. Harrington, T.J.; Gild, J.; Sarker, P.; Toher, C.; Rost, C.M.; Dippo, O.F.; McElfresh, C.; Kaufmann, K.; Marin, E.; Borowski, L.; et al. Phase stability and mechanical properties of novel high entropy transition metal carbides. *Acta Mater.* **2019**, *166*, 271–280. [\[CrossRef\]](#)
17. Feng, L.; Fahrenholtz, W.G.; Hilmas, G.E. Low-temperature sintering of single-phase, high-entropy carbide ceramics. *J. Am. Ceram. Soc.* **2019**, *102*, 7217–7224. [\[CrossRef\]](#)
18. Wei, X.; Liu, J.; Li, F.; Qin, Y.; Liang, Y.; Zhang, G. High entropy carbide ceramics from different starting materials. *J. Eur. Ceram. Soc.* **2019**, *39*, 2989–2994. [\[CrossRef\]](#)

19. Jin, T.; Sang, X.; Unocic, R.R.; Kinch, R.T.; Liu, X.; Hu, J.; Liu, H.; Dai, S. Mechanochemical-Assisted Synthesis of High-Entropy Metal Nitride via a Soft Urea Strategy. *Adv. Mater.* **2018**, *30*, 1707512. [[CrossRef](#)]
20. Gild, J.; Braun, J.; Kaufmann, K.; Marin, E.; Harrington, T.; Hopkins, P.E.; Vecchio, K.; Luo, J. A high-entropy silicide: $(\text{Mo}_{0.2}\text{Nb}_{0.2}\text{Ta}_{0.2}\text{Ti}_{0.2}\text{W}_{0.2})\text{Si}_2$. *J. Mater.* **2019**, *5*, 337–343. [[CrossRef](#)]
21. Qin, Y.; Liu, J.; Li, F.; Wei, X.; Wu, H.; Zhang, G.J. A high entropy silicide by reactive spark plasma sintering. *J. Adv. Ceram.* **2019**, *8*, 148–152. [[CrossRef](#)]
22. Minh, N.Q. Ceramic fuel cells. *J. Am. Ceram. Soc.* **1993**, *76*, 563–588. [[CrossRef](#)]
23. Dąbrowa, J.; Olszewska, A.; Falkenstein, A.; Schwab, C.; Szymczak, M.; Zajusz, M.; Możdziej, M.; Mikula, A.; Zielińska, K.; Berent, K.; et al. An innovative approach to design SOFC air electrode materials: High entropy $\text{La}_{1-x}\text{Sr}_x(\text{Co,Cr,Fe,Mn,Ni})\text{O}_{3-\delta}$ ($x=0, 0.1, 0.2, 0.3$) perovskites synthesized by the sol–gel method. *J. Mater. Chem. A* **2020**, *8*, 24455–24468. [[CrossRef](#)]
24. Wang, N.; Cao, M.; He, Z.; Diao, C.; Zhang, Q.; Zhang, Y.; Dai, J.; Zeng, F.; Hao, H.; Yao, Z. Structural and dielectric behavior of giant permittivity $\text{SrNb}_x\text{Ti}_{1-x}\text{O}_3$ ceramics sintered in nitrogen atmosphere. *Ceram. Int.* **2016**, *42*, 13593–13600. [[CrossRef](#)]
25. Wang, Z.; Cao, M.; Zhang, Q.; Hao, H.; Yao, Z. Dielectric Relaxation in Zr-Doped SrTiO_3 Ceramics Sintered in N_2 with Giant Permittivity and Low Dielectric Loss. *J. Am. Ceram. Soc.* **2015**, *98*, 476–482. [[CrossRef](#)]
26. Wang, K.F.; Liu, J.M.; Ren, Z.F. ChemInform Abstract: Multiferroicity—The Coupling Between Magnetic and Polarization Orders. *Adv. Phys.* **2009**, *58*, 321–448. [[CrossRef](#)]
27. Eerenstein, W.; Mathur, N.D.; Scott, J.F. Multiferroic and Magnetoelectric Materials. *Nature* **2006**, *442*, 759–765. [[CrossRef](#)] [[PubMed](#)]
28. Bokov, A.A.; Ye, Z.G. Recent progress in relaxor ferroelectrics with perovskite structure. *J. Mater. Chem.* **2006**, *41*, 31–52. [[CrossRef](#)]
29. Yokokawa, H.; Sakai, N.; Kawada, T.; Dokiya, M. Chemical thermodynamic considerations in sintering of LaCrO_3 -based perovskites. *J. Electrochem. Soc.* **1991**, *138*, 1018–1027. [[CrossRef](#)]
30. Graham, H.C.; Davis, H.H. Oxidation/vaporization kinetics of Cr_2O_3 . *J. Am. Ceram. Soc.* **1971**, *54*, 89–93. [[CrossRef](#)]
31. Mori, M.; Yamamoto, T.; Ichikawa, T.; Takeda, Y. Dense sintered conditions and sintering mechanisms for alkaline earth metal (Mg, Ca and Sr)-doped LaCrO_3 perovskites under reducing atmosphere. *Solid State Ion.* **2002**, *148*, 93–101. [[CrossRef](#)]
32. Bhatt, H.; Bahadur, J.; Deo, M.N.; Ramanathan, S.; Pandey, K.K.; Sen, D.; Mazumder, S.; Sharma, S.M. Effects of calcination on microscopic and mesoscopic structures in Ca- and Sr-doped nano-crystalline lanthanum chromites. *J. Solid. State. Chem.* **2011**, *184*, 204–213. [[CrossRef](#)]
33. Ding, X.; Liu, Y.; Gao, L.; Guo, L. Effects of cation substitution on thermal expansion and electrical properties of lanthanum chromites. *J. Alloys Compd.* **2006**, *425*, 318–322. [[CrossRef](#)]
34. Simner, S.P.; Hardy, J.S.; Stevenson, J.W. Sintering and properties of mixed lanthanide chromites. *J. Electrochem. Soc.* **2001**, *148*, A351. [[CrossRef](#)]
35. Ga, A.; Yin, X.L.; Zhao, Q.; He, D.L.; Zhao, Y.; Chang, A.M. A study based on MgAl_2O_4 - LaCrO_3 composite ceramics for high temperature NTC thermistors. *J. Mater. Sci. Mater. Electron.* **2019**, *30*, 11117–11122. [[CrossRef](#)]
36. Luo, P.; Zhang, B.; Zhao, Q.; He, D.L.; Chang, A.M. Electrical characterization of $0.6\text{MgAl}_2\text{O}_4$ - $0.4\text{La}_{(1-x)}\text{Sr}_x\text{CrO}_3$ high temperature NTC thermistors. *J. Mater. Sci. Mater. Electron.* **2017**, *28*, 16036–16043. [[CrossRef](#)]
37. Oses, C.; Toher, C.; Curtarolo, S. High-entropy ceramics. *Nat. Rev. Mater.* **2020**, *5*, 295–309. [[CrossRef](#)]
38. Guo, M.; Zhang, F.; Miao, Y.; Liu, Y.; Gao, F. Preparation and Electrical Properties of High Entropy $\text{La}(\text{Co}_{0.2}\text{Cr}_{0.2}\text{Fe}_{0.2}\text{Mn}_{0.2}\text{Ni}_{0.2})\text{O}_3$ Perovskite Ceramics Powder. *J. Inorg. Mater.* **2021**, *36*, 431–435. [[CrossRef](#)]
39. Zhivulin, V.E.; Trofimov, E.A.; Gudkova, S.A.; Pashkeev, I.Y.; Vinnik, D.A. Polysubstituted High-Entropy $[\text{LaNd}](\text{Co}_{0.2}\text{Cr}_{0.2}\text{Fe}_{0.2}\text{Mn}_{0.2}\text{Ni}_{0.2})\text{O}_3$ Perovskites: Correlation of the Electrical and Magnetic Properties. *Nanomaterials* **2021**, *11*, 1014. [[CrossRef](#)]
40. Joly, V.L.J.; Joy, P.A.; Date, S.K.; Gopinath, C.S. Two ferromagnetic phases with different spin states of Mn and Ni in $\text{LaMn}_{0.5}\text{Ni}_{0.5}\text{O}_3$. *Phys. Rev. B* **2002**, *65*, 184416. [[CrossRef](#)]
41. Kumar, P.; Singh, R.K.; Sinha, A.; Singh, P. Effect of isovalent ion substitution on electrical and dielectric properties of LaCrO_3 . *J. Alloys Compd.* **2013**, *576*, 154–160. [[CrossRef](#)]
42. Tsai, K.Y.; Tsai, M.H.; Yeh, J.W. Sluggish diffusion in Co–Cr–Fe–Mn–Ni high-entropy alloys. *Acta Mater.* **2013**, *61*, 4887–4897. [[CrossRef](#)]
43. Moldschmidt, G.V. Die Gsetze der Krystallochemie. *Naturwissenschaften* **1926**, *14*, 477–485. [[CrossRef](#)]
44. Ramadass, N. ABO_3 -type oxides—Their structure and properties—A bird’s eye view. *J. Mater. Sci. Technol.* **1978**, *36*, 231–239. [[CrossRef](#)]
45. Sarkar, A.; Djenadic, R.; Wang, D.; Hein, C.; Kautenburger, R.; Clemens, O.; Hahn, H. Rare earth and transition metal based entropy stabilised perovskite type oxides. *J. Eur. Ceram. Soc.* **2018**, *38*, 2318–2327. [[CrossRef](#)]
46. Kolisetty, A.; Fu, Z.; Koc, R. Development of $\text{La}(\text{CrCoFeNi})\text{O}_3$ system perovskites as interconnect and cathode materials for solid oxide fuel cells. *Ceram. Int.* **2017**, *43*, 7647–7652. [[CrossRef](#)]
47. Koc, R.; Anderson, H.U. Liquid phase sintering of LaCrO_3 . *J. Eur. Ceram. Soc.* **1992**, *9*, 285–292. [[CrossRef](#)]
48. Pu, Y.; Zhang, Q.; Li, R.; Chen, M.; Du, X.; Zhou, S. Dielectric properties and electrocaloric effect of high-entropy $(\text{Na}_{0.2}\text{Bi}_{0.2}\text{Ba}_{0.2}\text{Sr}_{0.2}\text{Ca}_{0.2})\text{TiO}_3$ ceramic. *Appl. Phys. Lett.* **2019**, *115*, 223901. [[CrossRef](#)]
49. Kar, B.S.; Goswami, M.N.; Jana, P.C. Effects of lanthanum dopants on dielectric and multiferroic properties of BiFeO_3 - BaTiO_3 ceramics. *J. Alloys Compd.* **2021**, *861*, 157960. [[CrossRef](#)]

50. Zhang, W.; Dai, F.Z.; Xiang, H.; Zhao, B.; Wang, X.; Ni, N.; Karre, R.; Wu, S.; Zhou, Y. Enabling highly efficient and broadband electromagnetic wave absorption by tuning impedance match in high-entropy transition metal diborides (HE TMB₂). *J. Adv. Ceram.* **2021**, *10*, 1299–1316. [[CrossRef](#)]
51. Ni, B.; Zhang, X.; Zhen, R.; Qi, X. Dielectric and ferroelectric properties of A-site disordered high-entropy chalcogenide oxides. *J. Chin. Ceram. Soc.* **2022**, *50*, 1475–1480.
52. Boudad, L.; Taibi, M.; Belayachi, A.; Abd-lefdil, M. Elaboration, characterization, and giant dielectric permittivity in solid state synthesized Fe half-doped LaCrO₃ perovskite. *Mater. Today Proc.* **2022**, *58*, 1108–1113. [[CrossRef](#)]
53. Coşkun, M.; Polat, Ö.; Coşkun, F.M.; Durmuş, Z.; Çağlar, M.; Türüt, A. Frequency and temperature dependent electrical and dielectric properties of LaCrO₃ and Ir doped LaCrO₃ perovskite compounds. *J. Alloys Compd.* **2018**, *740*, 1012–1023. [[CrossRef](#)]
54. RJD. Tilley. *Understanding Solids: The Science of Materials*; John Wiley & Sons: Chichester, UK, 2004; pp. 256–616.
55. Quan, B.; Shi, W.; Ong, S.J.H.; Lu, X.; Wang, P.L.; Ji, G.; Guo, Y.; Zheng, L.; Xu, Z.J. Defect engineering in two common types of dielectric materials for electromagnetic absorption applications. *Adv. Funct. Mater.* **2019**, *29*, 1901236. [[CrossRef](#)]
56. Aamir, M.; Bibi, I.; Ata, S.; Jilani, K.; Majid, F.; Kamal, S.; Alwadai, N.; Raza, M.A.S.; Bashir, M.; Iqbal, S.; et al. Ferroelectric, dielectric, magnetic, structural and photocatalytic properties of Co and Fe doped LaCrO₃ perovskite synthesized via micro-emulsion route. *Ceram. Int.* **2021**, *47*, 16696–16707. [[CrossRef](#)]
57. Zarrin, N.; Husain, S.; Gaur, D.D.; Somvanshi, A.; Fatema, M. Dopant incited alterations in structural, morphological, optical, and dielectric properties of Er-doped LaCrO₃. *J. Mater. Sci.-Mater Electron.* **2020**, *31*, 3466–3478. [[CrossRef](#)]